AMSR Ocean Algorithm

Frank J. Wentz
Remote Sensing Systems

1. Overview and Background Information

1.1. Introduction

With the advent of well-calibrated satellite microwave radiometers, it is now possible to obtain long time series of geophysical parameters that are important for studying the global hydrologic cycle and the Earth's radiation budget. Over the world's oceans, these radiometers simultaneously measure profiles of air temperature and the three phases of atmospheric water (vapor, liquid, and ice). In addition, surface parameters such as the near-surface wind speed, the sea-surface temperature, and the sea ice type and concentration can be retrieved. A wide variety of hydrological and radiative processes can be studied with these measurements, including air-sea and air-ice interactions (i.e., the latent and sensible heat fluxes, fresh water flux, and surface stress) and the effect of clouds on radiative fluxes. The microwave radiometer is truly a unique and valuable tool for studying our planet.

This Algorithm Theoretical Basis Document (ATBD) focuses on the Advanced Microwave Scanning Radiometer (AMSR) that is scheduled to fly in December 2000 on the NASA EOS-PM1 platform. AMSR will measure the Earth's radiation over the spectral range from 7 to 90 GHz. Over the world's oceans, it will be possible to retrieve the four important geophysical parameters listed in Table 1. The rms accuracies given in Table 1 come from past investigations and on-going simulations that will be discussed. Rainfall can also be retrieved, which is discussed in a separate AMSR ATBD.

We are confident that the expected retrieval accuracies for wind, vapor, and cloud will be achieved. The Special Sensor Microwave Image (SSM/I) and the TRMM microwave imager (TMI) have already demonstrated that these accuracies can be obtained. The AMSR wind retrievals will probably be more accurate than that of SSM/I and less affected by atmospheric moisture. A comparison between sea surface temperatures (SST) from TMI with buoy measurements indicate an rms accuracy between 0.5 and 0.7 K. One should keep in mind that part of the error arises from the temporal and spatial mismatch between the buoy measurement and the 50 km satellite footprint. Furthermore, the satellite is measuring the temperature at the surface the ocean (about 1 mm deep) whereas the buoy is measuring the bulk temperature near 1 m below the surface. There are still some concerns with regards to the sea-surface temperature retrieval, which are discussed in Section 1.5.

This document is version 2 of the AMSR Ocean Algorithm ATBD. The primary difference between this version and the earlier version is that the emissivity model for the 10.7 GHz has been updated using data from TMI. In addition, there are several small updates to the radiative transfer model (RTM).

Table 1. Expected Retrieval Accuracy for the Ocean Products

Geophysical Parameter	Rms Accuracy
Sea-surface temperature T_S	0.5 K
Near-surface wind speed W	1.0 m/s
Vertically integrated (i.e., columnar) water vapor V	1.0 mm
Vertically integrated cloud liquid water L	0.02 mm

1.2. Objectives of Investigation

There are two major objectives of this investigation. The first is to develop an ocean retrieval algorithm that will retrieve T_S, W, V, and L to the accuracies specified in Table 1. These products will be of great value to the Earth science community. The second objective is to improve the radiative transfer model (RTM) for the ocean surface and non-raining atmosphere. The 6.9 and 10.7 GHz channels on AMSR will provide new information on the RTM at low frequencies. Experience has shown that these two objectives are closely linked. A better understanding of the RTM leads to more accurate retrievals. A better understanding of the RTM also leads to new remote sensing techniques such as using radiometers to measure the ocean wind vector.

1.3. Approach to Algorithm Development

Radiative transfer theory provides the relationship between the Earth's brightness temperature T_B (K) as measured by AMSR and the geophysical parameters T_S, W, V, and L. This ATBD addresses the inversion problem of finding T_S, W, V, and L given T_B. We place a great deal of emphasis on developing a highly accurate RTM. Most of our AMSR work thus far has been the development and refinement of the RTM. This work is now completed, and Section 2 describes the RTM in considerable detail.

The importance of the RTM is underscored by the fact that AMSR frequency, polarization, and incidence angle selection is not the same as previous satellite radiometers. Table 2 compares AMSR with other radiometer systems. Albeit some of the differences are small, they are still significant enough to preclude developing AMSR algorithms by simply using existing radiometer measurements. The differences in frequencies and incidence angle must be taken into account when developing AMSR algorithms.

2. Geophysical Model for the Ocean and Atmosphere

2.1. Introduction

The key component of the ocean parameter retrieval algorithm is the geophysical model for the ocean and atmosphere. It is this model that relates the observed brightness temperature (T_B) to the relevant geophysical parameters. In remote sensing, the specification of the geophysical model is sometimes referred to as the forward problem in contrast to the inverse problem of inverting the model to retrieve parameters. An accurate specification of the geophysical model is the crucial first step in developing the retrieval algorithm.

2.2. Radiative Transfer Equation

We begin by deriving the radiative transfer model for the atmosphere bounded on the bottom by the Earth's surface and on the top by cold space. The derivation is greatly simplified by using the absorption-emission approximation in which radiative scattering from large rain drops and ice particles is not included. Over the spectral range from 6 to 37 GHz, the absorption-emission approximation is valid for clear and cloudy skies and for light rain up to about 2 mm/h. The results of *Wentz and Spencer* [1997] indicate that only 3% of the SSM/I observations over the oceans viewed rain rates exceeding 2 mm/h. Thus, the absorption-emission model to be presented will be applicable to about 97% of the AMSR ocean observations.

In the microwave region, the radiative transfer equation is generally given in terms of the radiation brightness temperature (T_B), rather than radiation intensity. So we first give a brief discussion on the relationship between radiation intensity and T_B. Let P_λ denote the power within the wavelength range $d\lambda$, coming from a surface area dA, and propagating into the solid angle $d\Omega$. The specific intensity of radiation I_λ is then defined by

$$P_\lambda = I_\lambda \cos\theta_i \, d\lambda \, dA \, d\Omega \tag{1}$$

The specific intensity is in units of erg/s-cm^3-steradian. The angle θ_i is the incidence angle defined as the angle between the surface normal and the propagation direction. For a black body, I_λ is given by Planck's law to be [*Reif*, 1965]

$$I_\lambda = \frac{2hc^2}{\lambda^5 \left[\exp\left(hc/\lambda kT \right) - 1 \right]} \tag{2}$$

where c is the speed of light (2.998×10^{10} cm/s), h is Planck's constant (6.626×10^{-27} erg-s), k is Boltzmann's constant (1.381×10^{-16} erg/K), λ (cm) is the radiation wavelength, and T (K) is the temperature of the black body. Consider a surface that is emitting radiation with a specific intensity I_λ. Then the brightness temperature T_B for this surface is defined as the temperature at which a black body would emit the radiation having specific intensity I_λ. In the microwave region, the exponent in (2) is small compared to unity, and (2) can be easily inverted to give T_B in terms of I_ν.

$$T_B = \frac{\lambda^4 I_\lambda}{2kc} \tag{3}$$

This approximation is the well known Rayleigh Jeans approximation for $\lambda \gg hc/kT$.

In terms of T_B, the differential equation governing the radiative transfer through the atmosphere is

$$\frac{\partial T_B}{\partial s} = -\alpha(s)\left[T_B(s) - T(s) \right] \tag{4}$$

where the variable s is the distance along some specified path through the atmosphere. The terms $\alpha(s)$ and $T(s)$ are the absorption coefficient and the atmospheric temperature at position s. Equation (4) is simply stating that the change in T_B is due to (1) the absorption of radiation arriving at s and (2) to emission of radiation emanating from s. We let s = 0 denote the Earth's surface, and let s = S denote the top of the atmosphere (i.e., the elevation above which $\alpha(s)$ is essentially zero).

Two boundary conditions that correspond to the Earth's surface at the bottom and cold space at the top are applied to equation (4). The surface boundary conditions states that the upwelling brightness temperature at the surface $T_B\uparrow$ is the sum of the direct surface emission and the downwelling radiation that is scattered upward by the rough surface [*Peake*, 1959].

$$T_{B\uparrow}(\mathbf{k_i},0) = E(\mathbf{k_i})T_S + \frac{\sec\theta_i}{4\pi}\int\limits_0^{\pi/2}\sin\theta_s d\theta_s \int\limits_0^{2\pi} d\varphi_s\, T_{B\downarrow}(\mathbf{k_s},0)\big[\sigma_{o,c}(\mathbf{k_s},\mathbf{k_i})+\sigma_{o,\times}(\mathbf{k_s},\mathbf{k_i})\big] \tag{5}$$

where the first T_B argument denotes the propagation direction of the radiation and the second argument denotes the path length s. The unit propagation vectors $\mathbf{k_i}$ and $\mathbf{k_s}$ denote the direction of the upwelling and downwelling radiation, respectively. In terms of polar angles in a coordinate system having the z-axis normal to the Earth's surface, these propagation vectors are given by

$$\mathbf{k_i} = \big[\cos\varphi_i\sin\theta_i, \sin\varphi_i\sin\theta_i, \cos\theta_i\big] \tag{6a}$$

$$\mathbf{k_s} = -\big[\cos\varphi_s\sin\theta_s, \sin\varphi_s\sin\theta_s, \cos\theta_s\big] \tag{6b}$$

The first term in (5) is the emission from the surface, which is the product of the surface temperature T_S and the surface emissivity $E(\mathbf{k_i})$. The second term is the integral of downwelling radiation $T_{B\downarrow}(\mathbf{k_s})$ that is scattered in direction $\mathbf{k_i}$. The integral is over the 2π steradian of the upper hemisphere. The rough surface scattering is characterized by the bistatic normalized radar cross sections (NRCS) $\sigma_{o,c}(\theta_s,\theta_i)$ and $\sigma_{o,\times}(\theta_s,\theta_i)$. These cross sections specify what fraction of power coming from $\mathbf{k_s}$ is scattered into $\mathbf{k_i}$. The subscripts c and $\times$ denote co-polarization (i.e., incoming and outgoing polarization are the same) and cross-polarization (i.e., incoming and outgoing polarizations are orthogonal), respectively. The cross sections also determine the surface reflectivity $R(\mathbf{k_i})$ via the following integral.

$$R(\mathbf{k_i}) = \frac{\sec\theta_i}{4\pi}\int\limits_0^{\pi/2}\sin\theta_s d\theta_s \int\limits_0^{2\pi} d\varphi_s\big[\sigma_{o,c}(\mathbf{k_s},\mathbf{k_i})+\sigma_{o,\times}(\mathbf{k_s},\mathbf{k_i})\big] \tag{7}$$

The surface emissivity $E(\mathbf{k_i})$ is given by Kirchhoff's law to be

$$E(\mathbf{k_i}) = 1 - R(\mathbf{k_i}) \tag{8}$$

It is important to note that equations (5) an (7) provide the link between passive microwave radiometry and active microwave scatterometry. The scatterometer measures the radar backscatter coefficient, which is simply $\sigma_{o,c}(-\mathbf{k_i},\mathbf{k_i})$.

The upper boundary condition for cold space is

$$T_{B\downarrow}(\mathbf{k_s},S) = T_C \tag{9}$$

This simply states that the radiation coming from cold space is isotropic and has a magnitude of $T_C = 2.7$ K.

The differential equation (4) is readily solved by integrating and applying the two boundary conditions (5) and (9). The result for the upwelling brightness temperature at the top of the atmosphere (i.e., the value observed by Earth-orbiting satellites) is

$$T_{B\uparrow}(\mathbf{k_i},S) = T_{BU} + \tau[ET_S + T_{B\Omega}] \tag{10}$$

where T_{BU} is the contribution of the upwelling atmospheric emission, τ is the total transmittance from the surface to the top of the atmosphere, E is the Earth surface emissivity given by (8), and $T_{B\Omega}$ is the surface scattering integral in (5). The atmospheric terms can be expressed in terms of the transmittance function $\tau(s_1,s_2)$

$$\tau(s_1,s_2) = \exp\left(-\int\limits_{s_1}^{s_2} ds\,\alpha(s)\right) \tag{11}$$

which is the transmittance between points s_1 and s_2 along the propagation path $\mathbf{k_s}$ or $\mathbf{k_i}$. The total transmittance τ in (10) is given by

$$\tau = \tau(0,S) \tag{12}$$

and the upwelling and downwelling atmosphere emissions are given by

$$T_{BU} = \int\limits_0^S ds\,\alpha(s)\,T(s)\,\tau(s,S) \tag{13a}$$

$$T_{BD} = \int\limits_0^S ds\,\alpha(s)\,T(s)\,\tau(0,s) \tag{13b}$$

The sky radiation scattering integral is

$$T_{B\Omega} = \frac{\sec\theta_i}{4\pi}\int\limits_0^{\pi/2}\sin\theta_s d\theta_s \int\limits_0^{2\pi} d\varphi_s(T_{BD}+\tau T_C)\big[\sigma_{o,c}(\mathbf{k_s},\mathbf{k_i})+\sigma_{o,\times}(\mathbf{k_s},\mathbf{k_i})\big] \tag{14}$$

Thus, given the temperature T_S and absorption coefficient α at all points in the atmosphere and given the surface bistatic cross sections, T_B can be rigorously calculated. However, in practice, the 3-dimensional specification of T_S and α over the entire volume of the atmosphere is not feasible, and to simplify the problem, the assumption of horizontal uniformity is made. That is to say, the absorption is assumed to only be a function of the altitude h above the Earth's surface, i.e., $\alpha(s) = \alpha(h)$. To change the integration variable from ds to dh, we note that for the spherical Earth

$$\frac{\partial s}{\partial h} = \frac{1 + \delta}{\sqrt{\cos^2 \theta + \delta(2 + \delta)}} \tag{15}$$

where θ is either θ_i or θ_s, $\delta = h/R_E$, and R_E is the radius of the Earth. In the troposphere $\delta << 1$, and an excellent approximation for $\theta < 60°$ is,

$$\frac{\partial s}{\partial h} = \sec \theta \tag{16}$$

With this approximation and the assumption of horizontal uniformity, the above equations reduce to the following expressions.

$$\boldsymbol{t}(h_1, h_2, \boldsymbol{q}) = \exp\left(-\sec \boldsymbol{q} \int_{h_1}^{h_2} dh\ \boldsymbol{a}(h)\right) \tag{17}$$

$$\boldsymbol{t} = \boldsymbol{t}(0, H, \boldsymbol{q}_i) \tag{18}$$

$$T_{BU} = \sec \boldsymbol{q}_i \int_0^H dh\ \boldsymbol{a}(h)\ T(h)\ \boldsymbol{t}(h, H, \boldsymbol{q}_i) \tag{19a}$$

$$T_{BD} = \sec \boldsymbol{q}_s \int_0^H dh\ \boldsymbol{a}(h)\ T(h)\ \boldsymbol{t}(0, h, \boldsymbol{q}_s) \tag{19b}$$

Thus, the brightness temperature computation now only requires the vertical profiles of T(h) and $\alpha(h)$ along with the surface cross sections. The following two sections discuss the atmospheric model for $\alpha(h)$ and the sea-surface model for the cross sections, respectively. In closing, we note that the AMSR incidence angle is 55° and hence approximation (16) is quite valid, with one exception. In the scattering integral, θ_s goes out to 90°, and in this case we use (15) to evaluate the integral.

2.3. Model for the Atmosphere

In the microwave spectrum below 100 GHz, atmospheric absorption is due to three components: oxygen, water vapor, and liquid water in the form of clouds and rain [*Waters*, 1976]. The sum of these three components gives the total absorption coefficient (napers/cm).

$$\alpha(h) = \alpha_O(h) + \alpha_V(h) + \alpha_L(h) \tag{20}$$

Numerous investigators have studied the dependence of the oxygen and water vapor coefficients on frequency ν (GHz), temperature T (K), pressure P (mb), and water vapor density ρ_V (g/cm^3) [*Becker and Autler*, 1946; *Rozenkranz*, 1975; *Waters*, 1976; *Liebe*, 1985]. To specify α_O and α_V as a function of (ν,T,P,ρ_V) we use the *Liebe* [1985] expressions with one modification. The self-broadening component of the water vapor continuum is reduced by a factor of 0.52 (see below). The liquid water coefficient α_L comes directly from the Rayleigh approximation to Mie scattering and is a function of T and the liquid water density ρ_L (g/cm^2) (see below). Figure 3 shows the total atmospheric absorption for each component. Results for three water vapor cases (10, 30, and 60 mm) are shown. The cloud water content is 0.2 mm. This corresponds to a moderately heavy non-raining cloud layer.

Let A_I denote the vertically integrated absorption coefficient.

$$A_I = \int_0^H dh\ \boldsymbol{a}_I(h) \tag{21}$$

where h is the height (cm) above the Earth's surface and subscript I equals O, V, or L. Equations (17) and (18) then give the total transmittance to be

$$\boldsymbol{t} = \exp\left[-\sec \boldsymbol{q}_i (A_O + A_V + A_L)\right] \tag{22}$$

Assuming for the moment that the atmospheric temperature is constant, i.e., T(h) = T, then the integrals in equations (19) can be exactly evaluated in closed form to yield

$$T_{BU} = T_{BD} = (1 - t)T \tag{23}$$

In reality, the atmospheric temperature does vary with h, typically decreasing at a lapse rate of about -5.5 C/km in the lower to mid troposphere. In view of (23), we find it convenient to parameterize the atmospheric model in terms of the following upwelling and downwelling effective air temperatures:

$$T_U = T_{BU} / (1 - \tau) \tag{24a}$$

$$T_D = T_{BD} / (1 - \tau) \tag{24b}$$

These effective temperatures are indicative of the air temperature averaged over the lower to mid troposphere. Note that in the absence of significant rain, T_U and T_D are very similar in value, with T_U being 1 to 2 K colder.
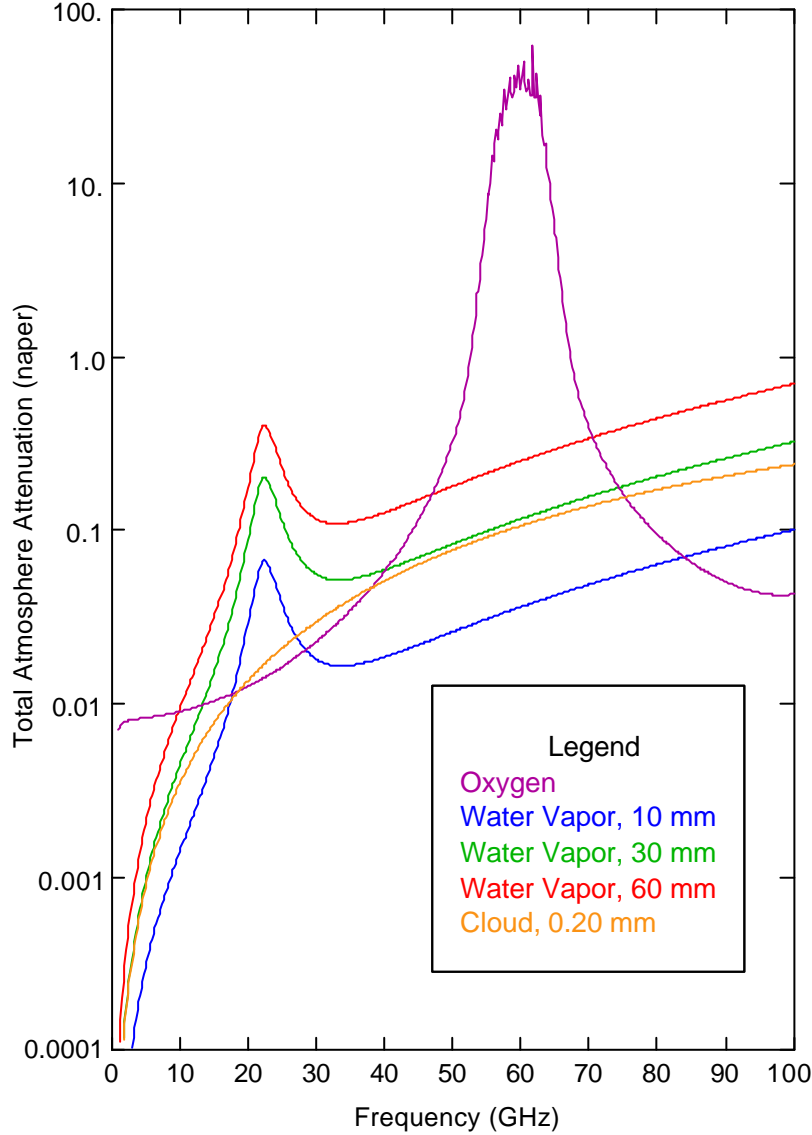

Fig. 3. The atmospheric absorption spectrum for oxygen, water vapor, and cloud water. Results for three water vapor cases (10, 30, and 60 mm) are shown. The cloud water content is 0.2 mm which corresponds to a moderately heavy non-raining cloud layer.

In view of the above equations, one sees that the atmospheric model can be parameterized in terms of the following 5 parameters:
1. Upwelling effective temperature T_U
2. Downwelling effective temperature T_D
3. Vertically integrated oxygen absorption A_O
4. Vertically integrated water vapor absorption A_V
5. Vertically integrated liquid water absorption A_L

To study the properties of the first four parameters, we use a large set of 42,195 radiosonde flights launched from small islands [Wentz, 1997]. These radiosonde reports provide air temperature T(h), air pressure p(h), and water

vapor density $\rho_V(h)$ at a number of levels in the troposphere. From these data, the coefficients α_O and α_V are computed from the *Liebe* [1985] expressions, except that the water vapor continuum term is modified as discussed in the next paragraph. Performing the numerical integrations as indicated above, T_U, T_D, A_O, and A_V are found for each radiosonde flight. In addition, the vertically integrated water vapor V is also computed.

$$V = 10 \int_0^H dh \; \mathbf{r}_V(h) \tag{25}$$

where $\rho_V(h)$ is in units of g/cm^3, and the leading factor of 10 converts from g/cm^2 to mm.

Wentz [1997] computed A_V directly from collocated SSM/I and radiosonde observations. At 19, 22, and 37 GHz, the Liebe A_V was found to be 4%, 3%, and 20% higher than the SSM/I-derived value, respectively. To quote *Liebe* [1985]: 'Water vapor continuum absorption has been a major source of uncertainty in predicting millimeter wave attenuation rates, especially in the window ranges.' The frequency of 37 GHz is in a water vapor window and is most affected by the continuum. It should be noted that Liebe also needed to rely on combined radiometer-radiosonde measurements to infer the continuum in the 6 to 37 GHz region. Liebe's data set in this spectral region is rather limited and does not contain any 37 GHz observations. We believe the SSM/I method of deriving A_V is more accurate than Liebe's method, and hence adjust the *Liebe* [1985] water vapor spectrum so that it will agree with the SSM/I results. We find that very good agreement is obtained by reducing the self-broadening component of the water vapor continuum by a factor of 0.52. After this adjustment, the agreement at all three frequencies is within ± 1%.

Figure 4 shows the T_D values computed from the 42,195 radiosondes plotted versus V. Three frequencies are shown (19, 22, and 37 GHz), and the curves are quite similar. The solid lines in the figure show equation (26), and vertical bars show the ± one standard deviation of T_D derived from the radiosondes. For low to moderate values of V (0 to 40 mm), T_D increases with V, and above 40 mm, T_D reaches a relatively constant value of 287 K. The T_U versus V curves (not shown) are very similar except that T_U is 1 to 2 K colder. The following least-square regressions are found to be a good approximation of the T_D, T_U versus V relationship:

$$\tag{26a}$$

$$T_U = T_D + b_6 + b_7 V \tag{26b}$$

where

$$T_V = 273.16 + 0.8337\,V - 3.029 \times 10^{-5} V^{3.33} \qquad V \le 48 \tag{27a}$$

$$T_V = 301.16 \qquad V > 48 \tag{27b}$$

and

$$\varsigma(T_S - T_V) = 1.05 \cdot T_S - T_V \cdot 1 - \frac{(T_S - T_V)^2}{1200} \qquad |T_S - T_V| \le 20K \tag{27c}$$

$$\mathbf{V}(T_S - T_V) = \text{sign}(T_S - T_V) \cdot 14K \qquad |T_S - T_V| > 20K \tag{27d}$$

V is in units of millimeters and all temperatures are in units of Kelvin. When evaluating (26a), the expression is linearly extrapolated when V is greater than 58 mm. We have included a small additional term that is a function of the difference between the sea-surface temperature T_S and T_V, which represents the sea-surface temperature that is typical for water vapor V. The term $\mathbf{V}(T_S - T_V)$ accounts for the fact that the effective air temperature is typically higher (lower) for the case of unusually warm (cold) water. The T_V versus V relationship was obtained by regressing the climatology sea-surface temperature at the radiosonde site to V derived from the radiosondes. Over the full range of V, the rms error in approximation (26) is typically about 3 K. Table 4 gives the b_0 through b_7 coefficients for all 8 AMSR frequencies.

The vertically integrated oxygen absorption A_O is nearly constant over the globe, with a small dependence on the air temperature. We find the following expression to be a very good approximation for A_O:

$$A_O = a_{O1} + a_{O2}(T_D - 270) \tag{28}$$

Table 4 gives the a_O coefficients for the 8 AMSR frequencies, and Table 5 gives the rms error in this approximation for the 8 frequencies. At 23.8 GHz and below, the error is negligible, being 0.0003 napers or less. At 36.5 GHz, the error is still quite small, being 0.0008 napers. Note that 0.001 napers roughly corresponds to a T_B error of 0.5 K. For the 50.3 and 52.8 GHz oxygen band channels, the error is considerably larger, but (28) is not used for the oxygen band channels. Rather the oxygen band channels can be used to retrieve T_D.

Table 4. Model Coefficients for the Atmosphere

Freq. (GHz)	6.93E+0	10.65E+0	18.70E+0	23.80E+0	36.50E+0	50.30E+0	52.80E+0	89.00E+0
b_0 (K)	239.50E+0	239.51E+0	240.24E+0	241.69E+0	239.45E+0	242.10E+0	245.87E+0	242.58E+0
b_1 (K mm^{-1})	213.92E–2	225.19E–2	298.88E–2	310.32E–2	254.41E–2	229.17E–2	250.61E–2	302.33E–2
b_2 (K mm^{-2})	–460.60E–4	–446.86E–4	–725.93E–4	–814.29E–4	–512.84E–4	–508.05E–4	–627.89E–4	–749.76E–4
b_3 (K mm^{-3})	457.11E–6	391.82E–6	814.50E–6	998.93E–6	452.02E–6	536.90E–6	759.62E–6	880.66E–6
b_4 (K mm^{-4})	–16.84E–7	–12.20E–7	–36.07E–7	–48.37E–7	–14.36E–7	–22.07E–7	–36.06E–7	–40.88E–7
b_5	0.50E+0	0.54E+0	0.61E+0	0.20E+0	0.58E+0	0.52E+0	0.53E+0	0.62E+0
b_6 (K)	–0.11E+0	–0.12E+0	–0.16E+0	–0.20E+0	–0.57E+0	–4.59E+0	–12.52E+0	–0.57E+0
b_7 (K mm^{-1})	–0.21E–2	–0.34E–2	–1.69E–2	–5.21E–2	–2.38E–2	–8.78E–2	–23.26E–2	–8.07E–2
a_{O1}	8.34E–3	9.08E–3	12.15E–3	15.75E–3	40.06E–3	353.72E–3	1131.76E–3	53.35E–3
a_{O2} (K^{-1})	–0.48E–4	–0.47E–4	–0.61E–4	–0.87E–4	–2.00E–4	–13.79E–4	–2.26E–4	–1.18E–4
a_{V1} (mm^{-1})	0.07E–3	0.18E–3	1.73E–3	5.14E–3	1.88E–3	2.91E–3	3.17E–3	8.78E–3
a_{V2} (mm^{-2})	0.00E–5	0.00E–5	–0.05E–5	0.19E–5	0.09E–5	0.24E–5	0.27E–5	0.80E–5

Table 5. RMS Error in Oxygen and Water Vapor Absorption Approximation

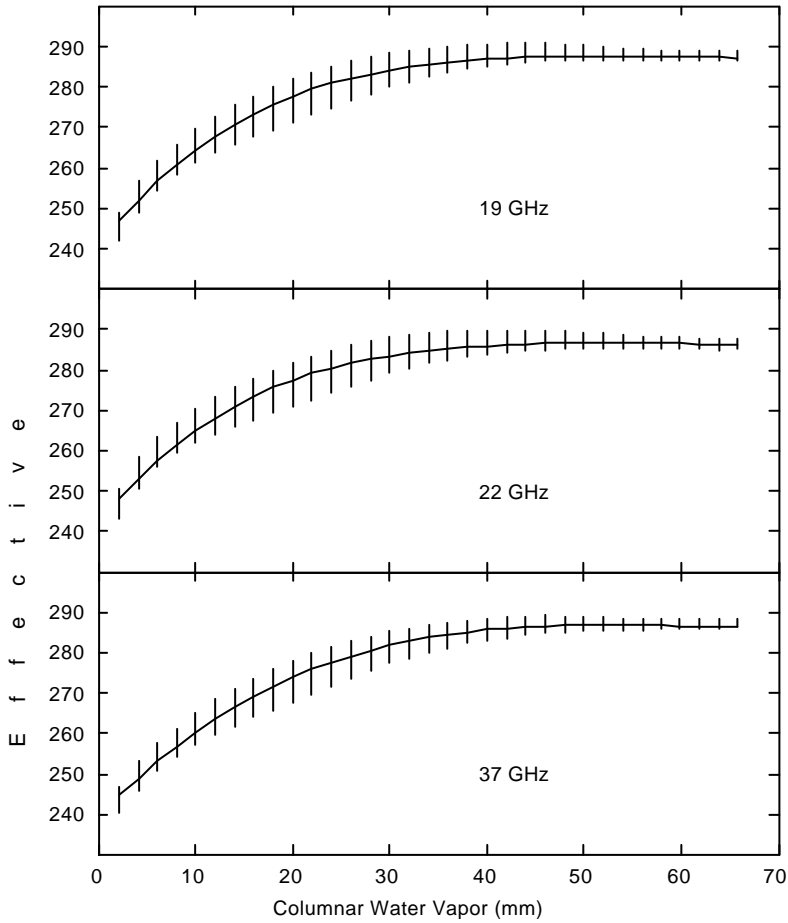| Freq. (GHz)	6.93	10.65	18.70	23.80	36.50	50.30	52.80	89.00
Oxygen, A_O	0.0002	0.0002	0.0003	0.0003	0.0008	0.0062	0.0163	0.0009
Vapor, A_V	0.0001	0.0002	0.0011	0.0013	0.0025	0.0042	0.0046	0.0129

Fig. 4. The effective air temperature T_D for downwelling radiation plotted versus the RAOB columnar water vapor. The solid curve is the model value, and the vertical bars are the ± one standard deviation of T_D derived from radiosondes.

The vapor absorption A_V is primarily a linear function of V, although there is a small second order term. We find the following expression is a good approximation for A_V:

$$A_V = a_{V1}V + a_{V2}V^2 \tag{29}$$

Table 4 gives the a_V coefficients for the 8 AMSR frequencies, and Table 5 gives the rms error in this approximation for the 8 frequencies. For the 6.9 and 10.7 AMSR channels, the rms error in this approximation is negligible, being 0.0002 napers or less. In the 18.7 to 36.5 range, the error remains relatively small (0.001 to 0.0025 napers), but not negligible.

The final atmospheric parameter to be specified is the vertically integrated liquid water absorption A_L. When the liquid water drop radius is small relative to the radiation wavelength, the absorption coefficient α_L (cm^{-1}) is given by the Rayleigh scattering approximation [*Goldstein*, 1951]:

$$\alpha_L = \frac{6\pi\rho_L(h)}{\lambda\rho_o}\mathrm{Im}\left(\frac{1-\varepsilon}{2+\varepsilon}\right) \tag{30}$$

where λ is the radiation wavelength (cm), $\rho_L(h)$ is the density (g/cm^3) of cloud water in the atmosphere given as a function of h, ρ_o is the density of water ($\rho_o \approx 1$ g/cm^3), and ε is the complex dielectric constant of water. Note that the dielectric constant varies with temperature and hence is also a function of h. Substituting (30) into (21) gives

$$A_L = \frac{0.6\pi L}{\lambda}\mathrm{Im}\left(\frac{1-\varepsilon}{2+\varepsilon}\right) \tag{31}$$

where L is the vertically integrated liquid water (mm) given by

$$L = 10\int_0^H dh\ \rho_L(h) \tag{32}$$

The leading factor of 10 converts from g/cm^2 to mm. In deriving (31), we have assumed the cloud is at a constant temperature. For the more realistic case of the temperature varying with height, ε should be evaluated at some mean effective temperature for the cloud. The specification of ε as a function of temperature and frequency is given in Section 2.4. An excellent approximation for (31) is found to be

$$A_L = a_{L1}\left[1 - a_{L2}(T_L - 283)\right]L \tag{33}$$

where T_L is the mean temperature of the cloud, and the a_L coefficients are given in Table 6 for the 8 AMSR frequencies. The error in this approximation is $\leq 1\%$ over the range of T_L from 273 to 288 K, which is negligible compared to other errors such as the uncertainty in specifying the cloud temperature T_L. Note that in the retrieval algorithm, the error in specifying T_L only effects the retrieved value of L. The retrieval of the other parameters only requires the spectral ratio of A_L, which is essentially independent of T_L due to the fact that a_{L2} is spectrally flat.

In the absence of rain, the cloud droplets are much smaller than the radiation wavelengths being considered, and equations (31) and (33) are valid. When rain is present, Mie scattering theory must be used to compute A_L. For light rain not exceeding 2 mm/h and for frequencies between 6 and 37 GHz, the Mie scattering computations give the following approximation [*Wentz and Spencer,* 1998]:

Table 6. Coefficients for Rayleigh Absorption and Mie Scattering.

Freq (GHz)	6.93	10.65	18.70	23.80	36.50	50.30	52.80	89.00
a_{L1}	0.0078	0.0183	0.0556	0.0891	0.2027	0.3682	0.4021	0.9693
a_{L2}	0.0303	0.0298	0.0288	0.0281	0.0261	0.0236	0.0231	0.0146
a_{L3}	0.0007	0.0027	0.0113	0.0188	0.0425	0.0731	0.0786	0.1506
a_{L4}	0.0000	0.0060	0.0040	0.0020	-0.0020	-0.0020	-0.0020	-0.0020
a_{L5}	1.2216	1.1795	1.0636	1.0220	0.9546	0.8983	0.8943	0.7961

$$A_R = a_{L3}\cdot\left[1 + a_{L4}\cdot(T_L - 283)\right]\cdot H\cdot R^{a_{L5}} \tag{34a}$$

The rain column height H (in km) can be approximated by:

$$H = 1 + 0.14\cdot(T_S - 273) - 0.0025\cdot(T_S - 273)^2 \qquad \text{if}\quad T_S < 301 \tag{34b}$$

$$H = 2.96 \qquad \text{if}\quad T_S \geq 301, \tag{34c}$$

where T_S denotes the sea surface temperature (in K). The rain rate R (in mm/h) is related to the liquid cloud water density L by

$$L = 0.18 \cdot 1 + \sqrt{HR} \,. \tag{34d}$$

In deriving (34a) we have used a *Marshall and Palmer* [1948] drop size distribution.

2.4. Dielectric Constant of Sea-Water and the Specular Sea Surface

A key component of the sea-surface model is the dielectric constant ε of sea water. The parameter is a complex number that depends on frequency ν, water temperature T_S, and water salinity s. The dielectric constant is given by [*Debye*,1929; *Cole and Cole*, 1941] as

$$\varepsilon = \varepsilon_\infty + \frac{\varepsilon_S - \varepsilon_\infty}{1 + [j\lambda_R / \lambda]^{1-\eta}} - \frac{2j\sigma\lambda}{c} \tag{35}$$

where $j = \sqrt{-1}$, λ (cm) is the radiation wavelength, ε_∞ is the dielectric constant at infinite frequency, ε_S is the dielectric constant for zero frequency (i.e., the static dielectric constant), and λ_R (cm) is the relaxation wavelength. The spread factor η is an empirical parameter that describes the distribution of relaxation wavelengths. The last term accounts for the conductivity of salt water. In this term, σ (sec^{-1}, Gaussian units) is the ionic conductivity and c is the speed of light.

Several investigators have developed models for the dielectric constant of sea water. In the *Stogryn* [1971] model the salinity dependence of ε_S and λ_R was based on the *Lane and Saxton* [1952] laboratory measurements of saline solutions. Stogryn noted that the Lane- Saxton measurements for distilled water did not agree with those of other investigators. The *Klein and Swift* [1977] model is very similar to Stogryn model except that the salinity dependence of ε_S was based on more recent 1.4 GHz measurements [*Ho and Hall*, 1973; *Ho et al.,* 1974]. Klein-Swift noted that their ε_S was significantly different from that derived from the Lane and Saxton measurements. It appears that there may be a problem with Lane-Saxton measurements. However, in the Klein-Swift model, the salinity dependence of λ_R was still based on the Lane-Saxton measurements. We analyzed all the measurements used by Stogryn and Klein-Swift and concluded that the Lane-Saxton measurements of ε for both distilled water and salt water were inconsistent with the results reported by all other investigators. Therefore, we completely exclude the Lane-Saxton measurements from our model derivation.

The model to be presented is very similar to the Klein-Swift model, with two exceptions. First, since we excluded Lane-Saxton measurements, the salinity dependence of λ_R is different. For cold water (0 to 10 C), our λ_R is about 5% lower than the Klein-Swift value and for warm water (30 C), it is about 1% higher. Second, our value for ε_∞ is 4.44 and the Klein-Swift value is 4.9, which was the value used by Stogryn. In the Stogryn model, $\eta = 0$, whereas in the Klein-Swift model, $\eta = 0.02$. *Grant et al.* [1957] pointed out that the choice of ε_∞ depends on the choice for η, where $\eta = 0 \rightarrow \varepsilon_\infty = 4.9$ and $\eta = 0.02 \rightarrow \varepsilon_\infty = 4.5$. Thus the Klein-Swift value of $\varepsilon_\infty = 4.9$ is probably too high. In terms of brightness temperatures, these λ_R and ε_∞ differences are most significant at the higher frequencies. For example, at 37 GHz and $\theta_i = 55°$, the difference in specular brightness temperatures produced by our model and the Klein-Swift model differ by about ± 2 K. Analyses of SSM/I observations show that our new model, as compared to the Klein-Swift model, produces more consistent retrievals of ocean parameters. For example, using the Klein-Swift model resulted in an abundance of negative cloud water retrievals in cold water. This problem no longer occurs with the new model. (The negative cloud water problem was the original motivation for doing this reanalysis of the ε model.)

We first describe the dielectric constant model for distilled water, and then extend the model to the more general case of a saline solution. The static dielectric constant ε_{S0} for distilled water has been measured by many investigators. The more recent measurements [*Malmberg and Maryott,* 1956; *Archer and Wang*, 1990] are in very good agreement (0.2%). The *Archer and Wang* [1990] values for ε_{S0}, which are reported in the *Handbook of Chemistry and Physics* [*Lide*,1993], are regressed to the following expression:

$$\varepsilon_{S0} = 87.90 \exp(-0.004585 \, t_S) \tag{36}$$

where t_S is the water temperature in Celsius units. The accuracy of the regression relative to the point values for ε_{S0} is 0.01% over the range from 0 to 40 C.

The other three parameters for the dielectric constant of distilled water are the relaxation wavelength λ_{R0}, the spread factor η, and ε_∞. We determine these parameters by a least-squares fit of (35) to laboratory measurements ε_{mea} of the dielectric constant for the range from 1 to 40 GHz. A literature search yielded ten papers reporting ε_{mea} for distilled water. Values for λ_{R0}, η, and ε_∞ are found so as to minimize the following quantity:

$$Q = [\mathrm{Re}(\varepsilon - \varepsilon_{mea})]^2 + [\mathrm{Im}(\varepsilon - \varepsilon_{mea})]^2 \tag{37}$$

The relaxation wavelength is a function of temperature [*Grant et al.,* 1957], but it is generally assumed that η and ε_∞ are independent of temperature. The least squares fit yields $\eta = 0.012$, $\varepsilon_\infty = 4.44$, and

$$\lambda_{R0} = 3.30 \ \exp(-0.0346 \ t_s + 0.00017 \ t_s^2) \tag{38}$$

These values are in good agreement with those obtained by other investigators. Our λ_{R0} agrees with the expression derived by *Stogryn* [1971] to within 1%. The values for η (ε_∞) reported in the literature vary from 0 to 0.02 (4 to 5). Note that using a larger value for η necessitates using a smaller value for ε_∞.

The presence of salt in the water produces ionic conductivity σ and modifies ε_S and λ_R. It is generally assumed that η and ε_∞ are not affected by salinity. *Weyl* [1964] found the following regression for the conductivity of sea water.

$$\boldsymbol{s} = 3.39 \times 10^9 \ C^{0.892} \exp(-\Delta_t \boldsymbol{z}) \tag{39}$$

$$\boldsymbol{z} = 2.03 \times 10^{-2} + 1.27 \times 10^{-4} \Delta_t + 2.46 \times 10^{-6} \Delta_t^2 - C \left(3.34 \times 10^{-5} - 4.60 \times 10^{-7} \Delta_t + 4.60 \times 10^{-8} \Delta_t^2\right) \tag{40}$$

$$C = 0.5536 \ s \tag{41}$$

$$\Delta_t = 25 - t_s \tag{42}$$

where s and C are salinity and chlorinity in units of parts/thousand. Note that we have converted the Weyl conductivity to Gaussian units of $\sec^{-1}$.

To determine the effect of salinity on ε_S, we use low frequency (1.43 and 2.65 GHz) measurements of ε for sea water and saline solutions [*Ho and Hall*, 1973; *Ho et al.,* 1974]. For the Ho-Hall data, only the real part of the dielectric constant is used in the fit. Klein and Swift reported that the measurements of the imaginary part were in error. To determine the effect of salinity on λ_R, we use higher frequency (3 to 24 GHz) measurements of ε for saline solutions [*Haggis et al.,* 1952; *Hasted and Sabeh*, 1953; *Hasted and Roderick,* 1958]. A least-squares fit to these data shows that the salinity dependence of ε_S and λ_R can be modeled as

$$\boldsymbol{e}_S = \boldsymbol{e}_{S0} \ \exp\left(-3.45 \times 10^{-3} s + 4.69 \times 10^{-6} s^2 + 1.36 \times 10^{-5} st_S\right) \tag{43}$$

$$\boldsymbol{l}_R = \boldsymbol{l}_{R0} - 6.54 \times 10^{-3} \left(1 - 3.06 \times 10^{-2} t_S + 2.0 \times 10^{-4} t_S^2\right) s \tag{44}$$

The accuracy of the dielectric constant model is characterized in terms of its corresponding specular brightness temperature T_B. For each laboratory measurement of ε, we compute the specular T_B for an incidence angle of 55° using the Fresnel equation (45) below. Two T_B's are computed: one using ε_{mea} and the other using the model ε coming from the above equations. For the low frequency Ho-Hall data, the rms difference between the 'measurement' T_B and the 'model' T_B is about 0.1 K for v-pol and 0.2 K for h-pol. For the higher frequency data set, the rms difference is 0.8 K for v-pol and 0.5 K for h-pol.

Once the dielectric constant is known, the v-pol and h-pol reflectivity coefficients ρ_V and ρ_H for a specular (i.e., perfectly flat) sea surface are calculated from the well-known Fresnel equations

$$\rho_v = \frac{\varepsilon \cos \theta_i - \sqrt{\varepsilon - \sin^2 \theta_i}}{\varepsilon \cos \theta_i + \sqrt{\varepsilon - \sin^2 \theta_i}} \tag{45a}$$

$$\rho_h = \frac{\cos \theta_i - \sqrt{\varepsilon - \sin^2 \theta_i}}{\cos \theta_i + \sqrt{\varepsilon - \sin^2 \theta_i}} \tag{45b}$$

where θ_I is the incidence angle. The power reflectivity R is then given by

$$R_{0p} = \left|\rho_p\right|^2 \tag{46}$$

where subscript 0 denotes that this is the specular reflectivity and subscript p denotes polarization.
An analysis using TMI data indicates small deviations from the model function for the dielectric constant of sea water as discussed above. The effect is mainly noted in the v-pol reflectivity. In order to account for these small differences a correction term of

$$\Delta R_{0V} = 4.887 \cdot 10^{-8} - 6.108 \cdot 10^{-8} \cdot T_S - 273^3$$

is added to the v-pol reflectivity R_{0v} in (46). The resulting changes in the brightness temperature range from about +0.14K in cold water to about –0.36K in warm water.

2.5. The Wind-Roughened Sea Surface

It is well known that the microwave emission from the ocean depends on surface roughness. A calm sea surface is characterized by a highly polarized emission. When the surface becomes rough, the emission increases

and becomes less polarized (except at incidence angles above 55º for which the vertically polarized emission decreases). There are three mechanisms that are responsible for this variation in the emissivity. First, surface waves with wavelengths that are long compared to the radiation wavelength mix the horizontal and vertical polarization states and change the local incidence angle. This phenomenon can be modeled as a collection of tilted facets, each acting as an independent specular surface [*Stogryn,* 1967]. The second mechanism is sea foam. This mixture of air and water increases the emissivity for both polarizations. Sea foam models have been developed by *Stogryn* [1972] and *Smith* [1988]. The third roughness effect is the diffraction of microwaves by surface waves that are small compared to the radiation wavelength. *Rice* [1951] provided the basic formulation for computing the scattering from a slightly rough surface. *Wu and Fung* [1972] and *Wentz* [1975] applied this scattering formulation to the problem of computing the emissivity of a wind-roughened sea surface.

These three effects can be parameterized in terms of the rms slope of the large-scale roughness, the fractional foam coverage, and the rms height of the small-scale waves. Each of these parameters depends on wind speed. *Cox and Munk* [1954], *Monahan and O'Muircheartaigh* [1980], and *Mitsuyasu and Honda* [1982] derived wind speed relationships for the three parameters, respectively. These wind speed relationships in conjunction with the tilt+foam+diffraction model provide the means to compute the sea-surface emissivity. Computations of this type have been done by *Wentz* [1975, 1983] and are in general agreement with microwave observations.

In addition to depending on wind speed, the large-scale rms slope and the small-scale rms height depend on wind direction. The probability density function of the sea-surface slope is skewed in the alongwind axis and has a larger alongwind variance than crosswind variance [*Cox and Munk*, 1954]. The rms height of capillary waves is very anisotropic [*Mitsuyasu and Honda*, 1982]. The capillary waves traveling in the alongwind direction have a greater amplitude than those traveling in the crosswind direction. Another type of directional dependence occurs because the foam and capillary waves are not uniformly distributed over the underlying structure of large-scale waves. *Smith's* [1988] aircraft radiometer measurements show that the forward plunging side of a breaking wave exhibits distinctly warmer microwave emissions than does the back side. In addition, the capillary waves tend to cluster on the downwind side of the larger gravity waves [*Cox*, 1958; *Keller and Wright*, 1975]. The dependence of foam and capillary waves on the underlying structure produces an upwind-downwind asymmetry in the sea-surface emissivity.

The anisotropy of capillary waves is responsible for the observed dependence of radar backscattering on wind direction [*Jones et al.,* 1977]. The upwind radar return is considerably higher than the crosswind return. Also, the modulation of the capillary waves by the underlying gravity waves causes the upwind return to be generally higher than the downwind return. These directional characteristics of the radar return have provided the means to sense wind direction from aircraft and satellite scatterometers [*Jones et al.,* 1979].

To model the rough sea surface, we begin by assuming the surface can be partitioned into foam-free areas and foam-covered areas within the radiometer footprint. The fraction of the total area that is covered by foam is denoted by f. The composite reflectivity is then given by

$$R = (1 - f)R_{clear} + f \kappa R_{clear} \tag{47}$$

where R_{clear} is the reflectivity of the rough sea surface clear of foam, and the factor κ accounts for the way in which foam modifies the reflectivity. As discussed above, foam tends to decrease the reflectivity, and hence $\kappa < 1$. The reflectivity of the clear, rough sea surface is modeled by the following equation:

$$R_{clear} = (1 - \beta) \ R_{geo} \tag{48}$$

where R_{geo} is the reflectivity given by the standard geometric optics model (see below) and the factor $1 - \beta$ accounts for the way in which diffraction modifies the geometric-optics reflectivity. *Wentz* [1975] showed that the inclusion of diffraction effects is a relatively small effect and hence β small compared to unity.

Combining the above two equations gives

$$R = (1 - F)R_{geo} \tag{49}$$

$$F = f + \beta - f\beta - f\kappa + f\kappa\beta \tag{50}$$

where F is a 'catch-all' term that accounts for both foam and diffraction effects. All of the terms that makeup F are small compared to unity, and the results to be presented show that F < 10%. The reason we lump foam and diffraction effects together is that they both are difficult to model theoretically. Hence, rather than trying to compute F theoretically, we let F be a model parameter that is derived empirically from various radiometer experiments. However, the R_{geo} term is theoretically computed from the geometric optics. Thus, the F term is a measure of that portion of the wind-induced reflectivity that is not explained by the geometric optics.

The geometric optics model assumes the surface is represented by a collection of tilted facets, each acting as an independent reflector. The distribution of facets is statistically characterized in terms of the probability density function $P(S_u, S_c)$ for the slope of the facets, where S_u and S_c are the upwind and crosswind slopes respectively.

Given this model, the reflectivity can be computed from equation (7). To do this, the integration variables θ_s, ϕ_s in (7) are transformed to the surface slope variables. The two equations governing this transformation are

$$\mathbf{k_s} = \mathbf{k_i} - 2(\mathbf{k_i} \cdot \mathbf{n})\mathbf{n} \tag{51}$$

$$\mathbf{n} = \frac{\left[-S_u, -S_c, 1\right]}{\sqrt{1 + S_u^2 + S_c^2}} \tag{52}$$

where $\mathbf{n}$ is the unit normal vector for a given facet. Transforming (7) to the S_u, S_c integration variables yields

$$R_{geo} = \frac{\int dS_u \int dS_c P(S_u, S_c)\sqrt{1 + S_u^2 + S_c^2}(\mathbf{k_i} \cdot \mathbf{n})\left|(\mathbf{p} \cdot \mathbf{h_i})r_h\mathbf{h_s} + (\mathbf{p} \cdot \mathbf{v_i})r_v\mathbf{v_s}\right|^2\left[\mathbf{c}(\mathbf{k_s})(1 - R_\times) + R_\times\right]}{\int dS_u \int dS_c P(S_u, S_c)\sqrt{1 + S_u^2 + S_c^2}(\mathbf{k_i} \cdot \mathbf{n})} \tag{53}$$

where $\mathbf{p}$ is the unit vector specifying the reflectivity polarization. The unit vectors $\mathbf{h_i}$ and $\mathbf{v_i}$ ($\mathbf{h_s}$ and $\mathbf{v_s}$) are the horizontal and vertical polarization vectors associated with the propagation vector $\mathbf{k_i}$ ($\mathbf{k_s}$) as measured in the tilted facet reference frame. These polarization vectors in the tilted frame of reference are given by

$$\mathbf{h_j} = \frac{\mathbf{k_j} \times \mathbf{n}}{\left|\mathbf{k_j} \times \mathbf{n}\right|} \tag{54a}$$

$$\mathbf{v_j} = \mathbf{k_j} \times \mathbf{h_j} \tag{54b}$$

where subscript $j = i$ or s. The terms ρ_v and ρ_h are the v-pol and h-pol Fresnel reflection coefficients given above. The last factor in (53) accounts for multiple reflection (i.e., radiation reflecting off of one facet and then intersecting another). $\chi(\mathbf{k_s})$ is the shadowing function given by *Wentz* [1975], and $R_\times$ is the reflectivity of the secondary intersection. The shadowing function $\chi(\mathbf{k_s})$ essentially equals unity except when $\mathbf{k_s}$ approaches surface grazing angles.

The interpretation of (53) is straightforward. The integration is over the ensemble of tilted facets having a slope probability of $P(S_u, S_c)$. The term $\sqrt{1 + S_u^2 + S_c^2}(\mathbf{k_i} \cdot \mathbf{n})$ is proportional to the solid angle subtended by the tilted facet as seen from the observation direction specified by $\mathbf{k_i}$. The term $\left|(\mathbf{p} \cdot \mathbf{h_i})r_h\mathbf{h_s} + (\mathbf{p} \cdot \mathbf{v_i})r_v\mathbf{v_s}\right|^2$ is the reflectivity of the tilted facet. And, the denominator in (53) properly normalizes the integral.

To specify the slope probability we use a Gaussian distribution as suggested by *Cox and Munk* [1954], and we assume that the upwind and crosswind slope variances are the same. Wind direction effects are considered in Section 2.7. Then, the slope probability is given by

$$P(S_u, S_c) = \left(\mathbf{p}\Delta S^2\right)^{-1}\exp\left[\frac{-S_u^2 - S_c^2}{\Delta S^2}\right] \tag{55}$$

where ΔS^2 is the total slope variance defined as the sum of the upwind and crosswind slope variances. Ocean waves with wavelengths shorter than the radiation wavelength do not contribute to the tilting of facets and hence should not be included in the ensemble specified by $P(S_u, S_c)$. For this reason, the effective slope variance ΔS^2 increases with frequency, reaching a maximum value referred to as the optical limit. The results of *Wilheit and Chang* [1980] and *Wentz* [1983] indicate that the optical limit is reached near $\nu = 37$ GHz. Hence, for $\nu \geq 37$ GHz, we use the *Cox and Munk* [1954] expression for optical slope variance. For lower frequencies, a reduction factor is applied to the Cox and Munk expression. This reduction factor is based on ΔS^2 values derived from the SeaSat SMMR observations [*Wentz*, 1983].

$$\Delta S^2 = 5.22 \times 10^{-3}\,W \qquad \nu \geq 37 \text{ GHz} \tag{56a}$$

$$\Delta S^2 = 5.22 \times 10^{-3}\left[1 - 0.00748(37 - \nu)^{1.3}\right]W \qquad \nu < 37 \text{ GHz} \tag{56b}$$

where W is the wind speed (m/s) measured 10 m above the surface. Note the Cox and Munk wind speed was measured at a 12.5 m elevation. Hence, their coefficient of 5.12×10^{-3} is increased by 2% to account for our wind being referenced to a 10 m elevation.

The sea-surface reflectivity R_{geo} is computed for a range of winds varying from 0 to 20 m/s, for a range of sea-surface temperatures varying from 273 to 303 K, and for a range of incidence angles varying from 49° to 57°. These computations require the numerical evaluation of the integral in equation (53). The integration is done over the range $S_u^2 + S_c^2 \leq 4.5\Delta S^2$. Facets with slopes exceeding this range contribute little to the integral, and it is not clear if a Gaussian slope distribution is even applicable for such large slopes. Analysis shows that the computed ensemble of R_{geo} is well approximated by the following regression:

$$R_{geo} = R_0 - [r_0 + r_1\theta_i - 53 + r_2 T_S - 288 + r_3\theta_i - 53 T_S - 288]W \qquad (57)$$

where the first term R_0 is the specular power reflectivity given by (46) and the second term is the wind-induced component of the sea-surface reflectivity. The r coefficients are given in Table 7 for all AMSR channels. Equation (57) is valid over the incidence angle from 49° to 57°. It approximates the θ_i and T_S variation of R_{geo} with an equivalent accuracy of 0.1 K. The approximation error in the wind dependence is larger. In the geometric optics computations, the variation of R_{geo} with wind is not exactly linear. In terms of T_B, the non-linear component of R_{geo} is about 0.1 K at the lower frequencies and 0.5 K at the higher frequencies. However, in view of the general uncertainty in the geometric optics model, we will use the simple linear expression for R_{geo}, and let the empirical F term account for any residual non-linear wind variations, as is discussed in the next paragraph.

In the case of the coefficients r_2 we do not use the geometric optics model coefficients (Table 7) but rather use the following empirically derived forms (units are s/m-K):

$$r_{2_{V-pol}} = -2.1 \cdot 10^{-5} \qquad (58)$$

$$r_{2_{h-pol}} = -5.5 \cdot 10^{-5} + 0.989 \cdot 10^{-6} \cdot 37 - v \qquad \text{if} \quad \boldsymbol{n} \le 37 \qquad (59a)$$

$$r_{2_{h-pol}} = -5.5 \cdot 10^{-5} \qquad \text{if} \quad \boldsymbol{n} > 37. \qquad (59b)$$

This accounts for the observations that the wind induced emissivity is less in warm water. This effect was observed during the monsoons in the Arabian sea.

Table 7. Model Coefficients for Geometric Optics

Freq. (GHz)	6.93E+0	10.65E+0	18.70E+0	23.80E+0	36.50E+0	50.30E+0	52.80E+0	89.00E+0
v-pol r_0	−0.27E−03	−0.32E−03	−0.49E−03	−0.63E−03	−1.01E−03	−1.20E−03	−1.23E−03	−1.53E−03
h-pol r_0	0.54E−03	0.72E−03	1.13E−03	1.39E−03	1.91E−03	1.97E−03	1.97E−03	2.02E−03
v-pol r_1	−0.21E−04	−0.29E−04	−0.53E−04	−0.70E−04	−1.05E−04	−1.12E−04	−1.13E−04	−1.16E−04
h-pol r_1	0.32E−04	0.44E−04	0.70E−04	0.85E−04	1.12E−04	1.18E−04	1.19E−04	1.30E−04
v-pol r_2	0.01E−05	0.11E−05	0.48E−05	0.75E−05	1.27E−05	1.39E−05	1.40E−05	1.15E−05
h-pol r_2	0.00E−05	−0.03E−05	−0.15E−05	−0.23E−05	−0.36E−05	−0.32E−05	−0.30E−05	0.00E−05
v-pol r_3	0.00E−06	0.08E−06	0.31E−06	0.41E−06	0.45E−06	0.35E−06	0.32E−06	−0.09E−06
h-pol r_3	0.00E−06	−0.02E−06	−0.12E−06	−0.20E−06	−0.36E−06	−0.43E−06	−0.44E−06	−0.46E−06
r_0 in units of s/m, r_1 in units of s/m-deg, r_2 in units of s/m-K, r_3 in units of s/m-deg-K								

In the 10-37 GHz band, the F term is found from collocated SSM/I-buoy and TMI-buoy observations. The procedure for finding F is essentially the same as described by *Wentz* [1997] for finding the wind-induced emissivity, but in this case we first remove the geometric optics contribution to R. The F term is found to be a monotonic function of wind speed described by

$$F = m_1 W \qquad\qquad W < W_1 \qquad (60a)$$
$$F = m_1 W + \tfrac{1}{2}(m_2 - m_1)(W - W_1)^2 / (W_2 - W_1) \qquad W_1 \le W \le W_2 \qquad (60b)$$
$$F = m_2 W - \tfrac{1}{2}(m_2 - m_1)(W_2 + W_1) \qquad\qquad W > W_2 \qquad (60c)$$

This equation represents two linear segments connected by a quadratic spline such that the function and its first derivative are continuous. The spline points are $W_1 = 3\,\text{m/s}$ and $W_2 = 12\,\text{m/s}$ for the v-pol and $W_1 = 7\,\text{m/s}$ and $W_2 = 12\,\text{m/s}$ for the h-pol , respectively. The m coefficients are found so that the T_B model matches the SSM/I observations in the and TMI observations when the buoy wind is used to specify W. For the lowest channel $\boldsymbol{n} = 6.9\,\text{GHz}$ no data exist yet and we have simply used the same values as for the $\boldsymbol{n} = 10.65\,\text{GHz}$ channel. This will be updated as soon as AMSR data become available. Table 8 summarizes the results for m_1 and m_2 at the 8 AMSR frequencies for v and h polarizations. Both coefficients flatten out and reach a maximum for $\boldsymbol{n} \ge 37$ GHz.

Table 8. The coefficients m_1 and m_2. Units are s/m.

Freq. (GHz)	6.93	10.65	18.70	23.80	36.50	50.30	52.80	89.00
v-pol m_1	0.00020	0.00020	0.00140	0.00178	0.00257	0.00260	0.00260	0.00260
h-pol m_1	0.00200	0.00200	0.00293	0.00308	0.00329	0.00330	0.00330	0.00330
v-pol m_2	0.00690	0.00690	0.00736	0.00730	0.00701	0.00700	0.00700	0.00700
h-pol m_2	0.00600	0.00600	0.00656	0.00660	0.00660	0.00660	0.00660	0.00660

These results indicate that diffraction plays a significant role in modifying the sea-surface reflectivity. If diffraction were not important, β would be 0 in equation (50), and F would be proportional to the fractional foam coverage f. Since f is essentially zero for W < 7 m/s, m_1 would be 0. This is not the case, and we interpret the m_1 coefficient as an indicator of diffraction.

2.6. Atmospheric Radiation Scattered by the Sea Surface

The downwelling atmospheric radiation incident on the rough sea surface is scattered in all directions. The scattering process is governed by the radar cross section coefficients σ_o as indicated by equation (14). For a perfectly flat sea surface, the scattering process reduces to simple specular reflection, for which radiation coming from the zenith angle θ_s is reflected into zenith angle θ_i, where $\theta_s = \theta_i$. In this case, the reflected sky radiation is simply RT_{BD}. However, for a rough sea surface, the tilted surface facets reflect radiation for other parts of the sky into the direction of zenith angle θ_i. Because the downwelling radiation T_{BD} increases as the secant of the zenith angle, the total radiation scattered from the sea surface is greater than that given by simple specular reflection. The sea-surface reflectivity model discussed in the previous section is used to compute the scattered sky radiation $T_{B\Omega}$. These computations show that $T_{B\Omega}$ can be approximated by

$$T_{B\Omega} = [(1+\Omega)(1-\tau)(T_D - T_C) + T_C] \ R \qquad (61)$$

where R is the sea-surface reflectivity given by (49), T_{BD} is the downwelling brightness temperature from zenith angle θ_i given by (24), and Ω is the fit parameter. The second term in the brackets is the isotropic component of the cold space radiation. This constant factor can be removed from the integral. The fit parameter for v-pol and h-pol is found to be

$$\Omega_V = [2.5 + 0.018(37 - \nu)][\Delta S^2 - 70.0\Delta S^6] \ \tau^{3.4} \qquad (62a)$$

$$\Omega_H = [6.2 - 0.001(37 - \nu)^2][\Delta S^2 - 70.0\Delta S^6] \ \tau^{2.0} \qquad (62b)$$

where ν is frequency (GHz) and ΔS^2 is the effective slope variance given by (56). The term $\Delta S^2 - 70.0\Delta S^6$ reaches a maximum at $\Delta S^2 = 0.069$. For $\Delta S^2 > 0.069$, the term is held at its maximum value of 0.046. Ω_V has a linear dependence on frequency, whereas Ω_H has a quadratic dependence, reaching a maximum value at $\nu = 37$ GHz. For $\nu > 37$ GHz, both Ω_V and Ω_H are held constant at their maximum values. Approximation (62) is valid for the range of incidence angles from 52° to 56°. For moderately high winds (12 m/s) and a moist atmosphere (high vapor and/or heavy clouds), the scattering process increases the reflected 37 GHz radiation by about 1 K for v-pol and 5 K for h-pol. At 7 GHz, the increase is much less, being about 0.2 K for v-pol and 0.8 K for h-pol. The accuracy of the above approximation as compared to the theoretical computation is about 0.03 K and 0.2 K at 7 and 37 GHz, respectively. Note that when the atmospheric absorption becomes very large (i.e., τ is small), Ω tends to zero because the sky radiation for a completely opaque atmosphere is isotropic.

2.7. Wind Direction Effects

The anisotropy of the sea-surface roughness produces a variation of the brightness temperature versus wind direction, as discussed in Section 2.5. In the 19 to 37 GHz band, *Wentz* [1992] determined this wind direction signal using collocated SSM/I T_B's and buoy wind vectors. At an incidence angle near 53°, the wind direction signal exhibits the following second-order harmonic variation with wind direction:

$$\Delta E_{19-37} = \gamma_1 \cos\phi + \gamma_2 \cos 2\phi \qquad (63)$$

where ΔE is the change in the sea-surface emissivity and ϕ is the wind-direction angle relative to the azimuth-look angle. When $\phi = 0°$ (180°), the observation is upwind (downwind). The subscript 19-37 denotes that the results are for the 19-37 GHz band. The amplitude coefficients γ_1 and γ_2 are found to be essentially the same for both 19 and 37 GHz. The coefficients are different for the two polarizations and do vary with wind speed as given below

$$\gamma_{1V} = \ \ 7.83 \times 10^{-4} W - 2.18 \times 10^{-5} W^2 \qquad (64a)$$

$$\gamma_{2V} = -4.46 \times 10^{-4} W + 3.00 \times 10^{-5} W^2 \qquad (64b)$$

$$\gamma_{1H} = 1.20 \times 10^{-3} \, W - 8.57 \times 10^{-5} \, W^2 \tag{65a}$$

$$\gamma_{2H} = -8.93 \times 10^{-4} \, W + 3.76 \times 10^{-5} \, W^2 \tag{65b}$$

In *Wentz* [1992], the wind direction signal was expressed in terms of a brightness temperature change rather than an emissivity change, and the wind speed was referenced to a 19.5 m anemometer height. In the above equations, we have converted the *Wentz* [1992] expressions from ΔT_B to ΔE and use a 10 m reference height for W.

Little is known about the wind direction signal for frequencies below 19 GHz. Some very preliminary data from the Japanese AMSR aircraft simulations suggests that the signal decreases with decreasing frequency. Other than this, there are no experimental data on the variation of T_B versus ϕ at 6.9 and 10.7 GHz. As an educated guess on what will be observed at these lower frequencies we reduce the wind direction signal from its value at 19 GHz by a factor of 0.82 at 10.7 GHz and by a factor of 0.62 at 6.9 GHz.

The result for the wind direction signal from (64) and (65) should be regarded as preliminary. Recent aircraft data *Yueh et al.* [1999] as well as a first analysis of TMI measurements suggest that at wind speeds below 8 m/s the wind direction signal is noticeably smaller than the one obtained from (64) and (65), especially for the h-pol. A reanalysis of the directional signal using data from 5 SSM/I satellites between 1987 and 1999 as well as recent TMI data is currently under way.

3. The Ocean Retrieval Algorithm

3.1 Introduction

In general, there are three types of ocean retrieval algorithms:
1. Multiple linear regression algorithms
2. Non-linear, iterative algorithms
3. Post-launch *in-situ* regression algorithms

The first two types are physical algorithms in the sense that radiative transfer theory is used in their derivation. The third type is purely statistical with little or no consideration of the underlying physics. We now describe each of these algorithms and discuss their strengths and weaknesses.

3.2 Multiple Linear Regression Algorithm

Consider a linear process in which a set of inputs denoted by the column vector **X** is transformed to a set of outputs denoted by the column vector **Y**. The linear process is then characterized by the matrix **A** that relates **Y** to **X**.

$$\mathbf{Y} = \mathbf{A}\mathbf{X} \tag{66}$$

The measurement of Y usually contains some noise **e** and is denoted by

$$\widetilde{\mathbf{Y}} = \mathbf{Y} + e = \mathbf{A}\mathbf{X} + e \tag{67}$$

The retrieval problem is then to estimate **X** given $\widetilde{\mathbf{Y}}$. The most commonly used criteria for estimating **X** is to find **X** such that the variance between **Y** and $\widetilde{\mathbf{Y}}$ is minimized. Using this criteria, one finds the well known least-squares solution:

$$\overrightarrow{\mathbf{X}} = (\mathbf{A}^T \Xi^{-1} \mathbf{A})^{-1} \mathbf{A}^T \Xi^{-1} \widetilde{\mathbf{Y}} \tag{68}$$

where **X** is the correlation matrix for the error vector **e**. If the errors are uncorrelated, then **X** is diagonal.

For our application, the system input vector **X** is the set of geophysical parameters **P** and the output vector $\widetilde{\mathbf{Y}}$ is the set of T_B measurements. Note that X and Y can be non-linear functions of P and T_B, respectively without violating the requirement for linearity between **X** and **Y**. For example, the relationship between T_B and atmospheric parameters V and L can be approximated by

$$T_B \approx T_E \left\{ 1 - R \, \exp\left[-2\sec\mathbf{q}_i \left(A_O + a_V V + a_L L \right) \right] \right\} \tag{69}$$

where T_E is an effective temperature of the ocean-atmosphere system which is relatively constant. Then,

$$\ln(T_E - T_B) = \ln(R T_E) - 2\sec\mathbf{q}_i \left(A_O + a_V V + a_L L \right) \tag{70}$$

From this we see that the relationship between T_B and V, L can be linearized by transforming from $\mathbf{Y} = T_B$ to $\mathbf{Y} = \ln(T_E - T_B)$. *Wilheit and Chang* [1980] followed this approach and used a value of 280 K for T_E. As a further extension, **Y** can also include higher order terms such as T_B^2 and $T_{B37V} T_{B23H}$.

Likewise, the input X can be a nonlinear transformation of the geophysical parameters P. For example, the wind speed dependence of T_B (i.e., $\partial T_B / \partial W$) increases with wind speed, and the relationship can be made linear by the following transformation

$$W' = W \qquad\qquad\qquad\qquad W < W_1 \qquad\qquad (71a)$$
$$W' = W + M_1 (W - W_1)^2 \qquad W_1 \leq W \leq W_2 \qquad (71b)$$
$$W' = M_2 W - M_3 \qquad\qquad\quad W > W_2 \qquad\qquad (71c)$$

This transformation represents two linear segments connected by a quadratic spline such that the function and its first derivative are continuous.

Thus the requirement of linearity is not as constraining as it might first appear, and a generalized linear statistical regression algorithm can be represented by

$$P_j = \Re\left[c_{0j} + \sum_{i=1}^{I} c_{ij} \Im(T_{Bi}) \right] \qquad (72)$$

where $\Im$ and $\Re$ are linearizing functions. Subscript i denotes the AMSR channel (1 = 6.9V, 2 = 6.9H, etc.), and subscript j denotes the parameter to be retrieved (1 = T_S, 2 = W, 3 = V, 4 = L). For AMSR, our initial design for the linear regression algorithm discussed in the next section uses the following linearizing functions:

$$\Im(T_B) = T_B \qquad\qquad\qquad \nu = 6.9 \text{ and } 10.7 \text{ GHz} \qquad (73a)$$
$$\Im(T_B) = -\ln(290 - T_B) \qquad \nu = 18.7, 23.8, \text{ and } 36.5 \text{ GHz} \qquad (73b)$$
$$\Re(X) = X \qquad\qquad\qquad\qquad\qquad\qquad\qquad (74)$$

After testing the initial algorithm, we will experiment with additional linearizing functions, such as the wind speed linearization given by (71).

In principle, the c_{ij} coefficients can be found from (68) given the **A** matrix and the error correlation matrix **X**. However, even after the linearizing functions are applied, the relationship of **Y** versus **X** is not strictly linear, and the elements of **A** matrix are not constant, but rather vary with **P**. One could find a linear approximation for the **Y** versus **X** relationship, and then derive the c_{ij} coefficients from (68). However, we prefer the more direct approach suggested by *Wilheit and Chang* [1980] in which brightness temperatures are computed for an ensemble of environmental scenes and then multiple linear regression is used to derive the c_{ij} coefficients, as is discussed in the following section.

3.3. Derivation and Testing of the Linear Regression Algorithm

The derivation of the c_{ij} coefficients in the AMSR linear regression algorithm is shown in Figure 5. A large ensemble of ocean-atmosphere scenes are first assembled. The specification of the atmospheres comes from 42,195 quality-controlled radiosonde flights launched from small islands during the 1987 to 1990 time period [*Wentz*, 1997]. One half of these radiosonde flights are used for deriving the c_{ij} coefficients, and the other half is withheld for testing the algorithm. A cloud layer of various columnar water densities ranging from 0 to 0.3 mm is superimposed on the radiosonde profiles. Underneath these simulated atmospheres, we place a rough ocean surface. The sea-surface temperature T_S is randomly varied from 0 to 30 C, the wind speed W is randomly varied from 0 to 20 m/s, and the wind direction ϕ is randomly varied from 0 to 360°. About 400,000 scenes are generated in this manner.

In nature, there is a strong correlation between T_S and W. We could have incorporated this correlation into the ensemble of the scene. For example, we could have discarded cases of very cold water and very high water vapor, which never occur in nature. However, for now we include these unrealistic cases in order to determine if the algorithm is
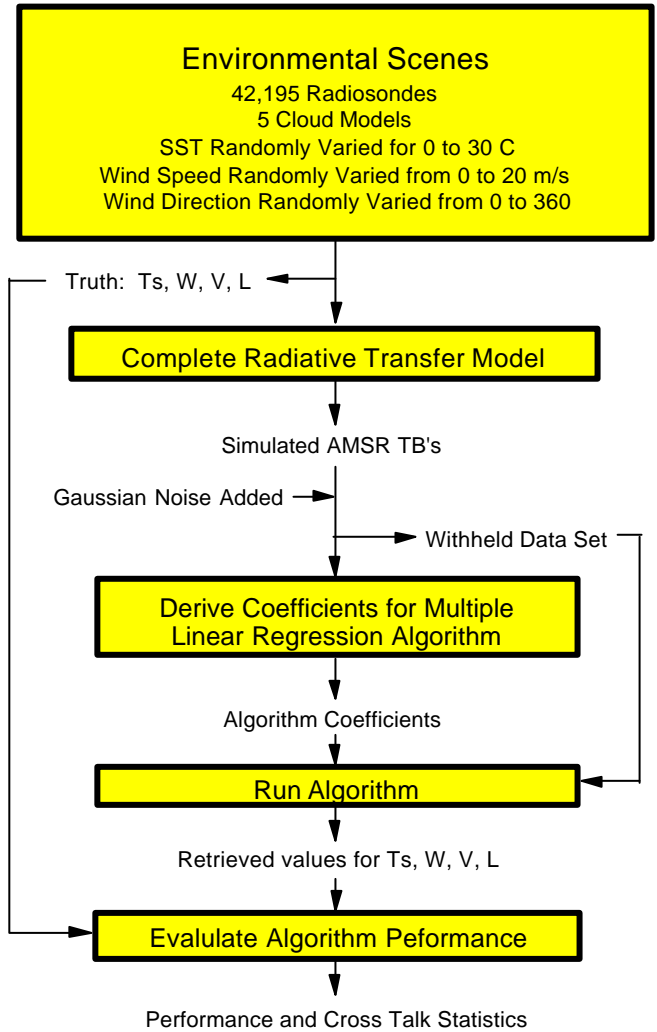

Fig. 5. Derivation and testing of the linear regression algorithm

truly capable of separating the T_S signal from the V signal.

Atmospheric brightness temperatures T_{BU} and T_{BD} and transmittance τ are computed from the radiosonde + cloud profiles of $T(h)$, $p(h)$, $\rho_V(h)$, and $\rho_L(h)$ using equations (17), (18) and (19). The reflectivity R of the rough sea surface is computed according to the equations given in Section 2.5, and the atmospheric radiation scattered from the sea surface $T_{B\Omega}$ is computed from (61). Wind direction effects are included as described in Section 2.7. Finally, the brightness temperature T_B as seen by AMSR is found by combining the atmospheric and sea-surface components, as is expressed by (10).

Noise is added to the simulated AMSR T_B's. This noise represents the measurement error in the AMSR T_B's. The measurement error depends on the spatial resolution. At a 60-km resolution, which is commensurate with the 6.9 GHz footprint, the measurement error is 0.1 K. A random number generator is used to produce Gaussian noise having a standard deviation of 0.1 K. This noise is added to the simulated T_B's. At this point in the simulation, we could also add modeling error to the T_B's. Modeling error accounts for the difference between the model and nature. It is a very difficult parameter to determine since it involves physical processes which are not sufficiently understood to be included in the current model. For now, we are not including any modeling error in the simulations, but we will be investigating this problem in the future.

Given the noise-added simulated T_B's, the standard multiple linear regression technique is used to find the c_{ij} coefficients. The coefficients are found such that the rms difference between P_j and the true value for the specified environmental scene is minimized. For the initial set of simulations, we use all 10 lower frequency channels (i.e., 6.9, 10.7, 18.7, 23.8 and 36.5 GHz, dual polarization). Later on, we will investigate the utility of using a reduced set of channels.

The algorithm is tested by repeating the above process, only this time using the withheld environmental scenes. The geophysical parameters T_S, W, V, and L are computed from the noise-added T_B's using equation (72). Statistics on the error in P_i are accumulated. The results are shown in Figure 6. The solid line in the figure shows the mean retrieval error, and the dashed lines show the one standard deviation envelope. The retrieval error for each of the four parameters is plotted versus the four parameters in order to show the crosstalk error matrix. The diagonal in the crosstalk matrix verifies that the dynamic range of a given parameter is correct, and the off-diagonal plots verify that there is no crosstalk error in the retrieval.

The results look quite good. There is a little crosstalk, but it is quite small. Table 9 gives the overall rms error for the retrievals. Wind direction variability is a major source of error in the T_S retrieval. When wind direction variability is removed from the simulations, the T_S retrieval error decreases to 0.3 C. The wind direction problem is further discussed in Sections 1.5 and 4.3.

We again emphasize that these results are very preliminary. There is much more work to do. For example, the cloud models need to be more variable and the performance of the relatively simple LSR algorithm needs to be compared with the non-linear algorithm discussed in the next section.

Table 9. Preliminary Estimate of Retrieval Error

Ocean Parameter	Rms Error
Sea-Surface Temperature	0.58 C
Wind Speed	0.86 m/s
Columnar Water Vapor	0.57 mm
Columnar Cloud Water	0.017 mm

3.4. Non-Linear, Iterative Algorithm

The major shortcoming of the multiple linear regression algorithm is that the non-linearities in the T_B versus **P** relationship are handled in an *ad hoc* manner. The linearization functions are only approximations, and the inclusion of second order terms such as T_B^2 and $T_{B37V} T_{B23H}$ do not really describe the inverse of the T_B versus **P** relationship. A more rigorous treatment of the non-linearity problem is to express the T_B versus **P** relationship in terms of a non-linear model function $F(\mathbf{P})$, and then invert the following set of equations

$$T_{Bi} = F_i(\mathbf{P}) + \varepsilon_i \tag{75}$$

where subscript i denotes the observation number and ε_i is the measurement noise. The number of observations must be equal to or greater than the number of unknown parameters (i.e., the number of elements in **P**). For each set of AMSR observations, equations (75) are inverted to yield **P**. This method is much more numerically intensive than the linear regression algorithm in which there is a fixed relationship between **P** and T_B. However, given today's computers, the computational burden is no longer a problem.

Equation (75) is solved using an extension of Newton's iterative method. In Newton's method, the model function is expressed as a Taylor expansion:

$$T_{Bi} = F_i(\overline{\mathbf{P}}) + \sum_{j=1}^{4} \left(P_j - \overline{P}_j\right)\frac{\partial F_i}{\partial P_j}\bigg|_{\overline{\mathbf{P}}} + O^2 + \mathbf{e}_i \qquad (76)$$
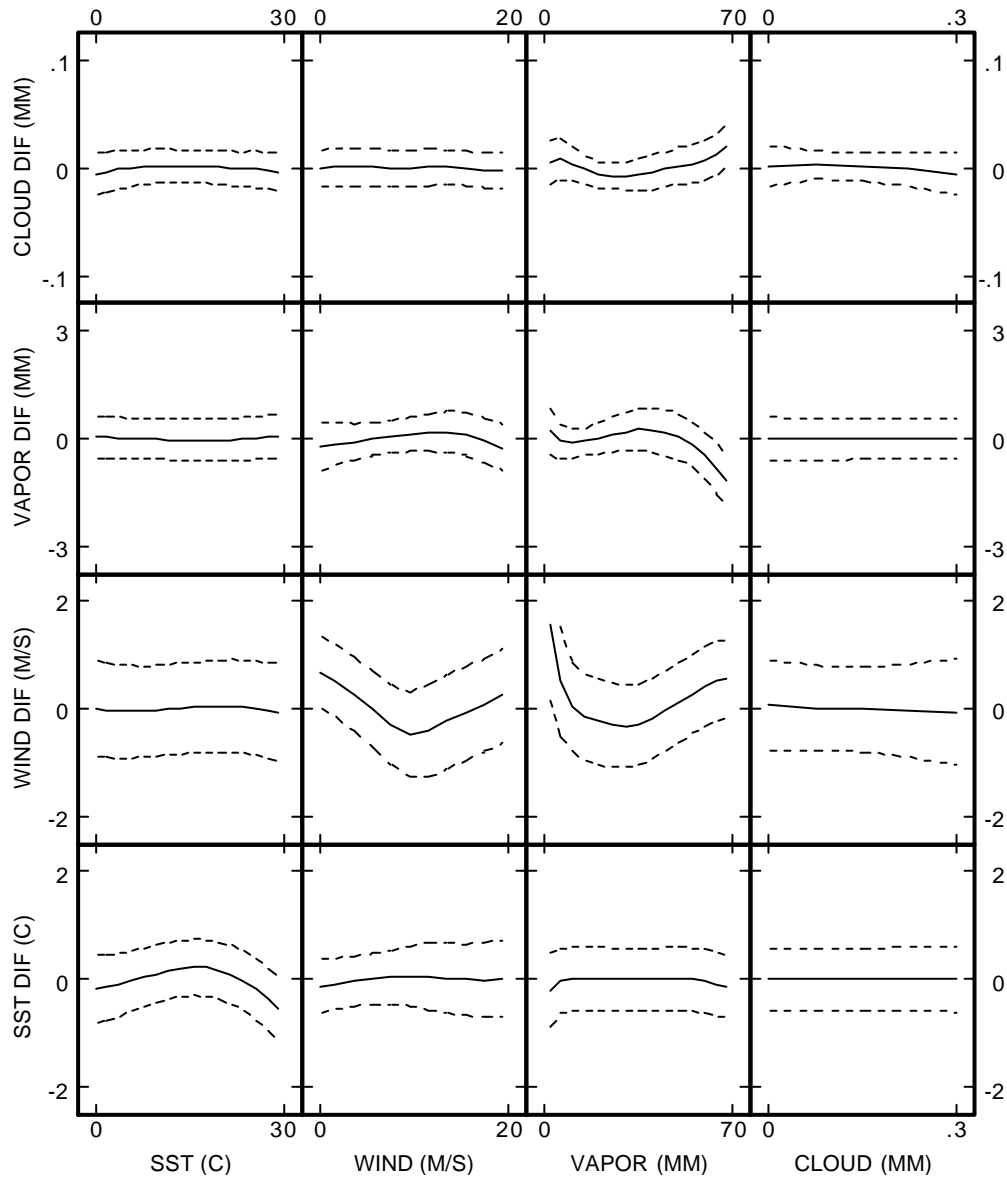

Fig 6. Preliminary results for the linear statistical regression algorithm for AMSR. The solid line in the figure shows the mean retrieval error, and the dashed lines show the one standard deviation envelope. The retrieval error for each of the four parameters is plotted versus the four parameters in order to show the crosstalk error matrix. The diagonal in the crosstalk matrix verifies that the dynamic range of a given parameter is correct, and the off-diagonal plots verifies that there is no crosstalk error in the retrieval.

where $\overline{\mathbf{P}}$ is a first guess value for $\mathbf{P}$ and O^2 represents the higher order terms in the expansion. This system of simultaneous equations is written in matrix form as

$$\Delta \mathbf{T_B} = \mathbf{A} \ \Delta\mathbf{P} + \mathbf{O}^2 + \mathbf{e} \tag{77}$$

where $\mathbf{A}$ is a matrix of $i \times j$ elements and $\mathbf{\Delta T_B}$, $\mathbf{\Delta P}$, and $\mathbf{e}$ are column vectors. The elements of $\mathbf{A}$, $\mathbf{\Delta T_B}$, and $\mathbf{\Delta P}$ are

$$A_{ij} = \left. \frac{\partial F_i}{\partial P_j} \right|_{\overline{\mathbf{P}}} \tag{78}$$

$$\Delta T_{Bi} = T_{Bi} - F_i(\overline{\mathbf{P}}) \tag{79}$$

$$\Delta P_j = P_j - \overline{P}_j \tag{80}$$

Equation (77) is solved by ignoring the higher order terms (i.e., by setting O^2 to zero), and the solution is

$$\mathbf{P} = \overline{\mathbf{P}} + (\mathbf{A^T \Xi^{-1} A})^{-1} \mathbf{A^T \Xi^{-1}} \Delta \mathbf{T_B} \tag{81}$$

where $\mathbf{\Xi}$ is the error correlation matrix. This procedure is then repeated with $\mathbf{P}$ from (81) replacing $\overline{\mathbf{P}}$, and several such iterations are performed. For the no-noise case ($\mathbf{e} = 0$), $\mathbf{\Xi}$ drops out of the formulation and an exact solution is obtained when $\mathbf{\Delta T_B}$ goes to zero. For the noise case, a solution is found when $\mathbf{\Delta T_B}$ reaches some constant minimum value.

The solution of P can be constrained by the inclusion of *a priori* information. This is accomplished by including additional equations in (77). For example, if ancillary information on wind direction were available, then the following equation could be added to (77)

$$\phi = \overline{\phi} + \varepsilon_\phi \tag{82}$$

where $\overline{\phi}$ is the a priori estimate of ϕ and ε_ϕ is the rms uncertainty in that estimate. Similar constraining equations can be included for other types of information such as the vertical distribution of water vapor and air temperature.

In general, there is no guarantee that a solution will be found using this method. Furthermore, if a solution is found, there is no guarantee that it is an unique solution. However for the case of AMSR, the relationships between $\mathbf{P}$ and T_B are quasi-linear in that $\partial T_B/\partial P > 0$ for all channels except 36.5 GHz in cold water, for which $\partial T_B/\partial T_S$ is < 0. Experience has shown that a solution is nearly always found. It also appears that this solution is unique, but this needs to be verified.

We have been assuming that the T_B versus $\mathbf{P}$ relationship can be exactly described by a non-linear model function F. In this case, the non-linear, iterative algorithm has the distinct advantage of finding the exact solution. In comparison, the $\mathbf{P}$ found by the linear regression algorithm would be in error by some degree due to the non-linearities. However, in practice it is not possible to exactly represent the T_B versus $\mathbf{P}$ relationship in terms a model function F($\mathbf{P}$). For example, the T_B not only depends on the columnar content of water vapor but also on vertical distribution of the vapor. Thus, some approximations need to be made when going from the integral equations of radiative transfer to a simplified model function F($\mathbf{P}$). These assumptions were discussed in length in Section 2. In the derivation of the linear regression algorithm, the complete integral formulation of the radiative transfer theory is used, and there is no need for the simplifying assumptions.

In comparing the two types of algorithms, there is a tradeoff between errors due to non-linearities in the linear regression algorithm and errors due to simplifying assumptions in the non-linear, iterative algorithm. Our plan is to develop and test both types of algorithms in parallel, compare their relative performance, and then select one or the other.

3.5. Post-Launch *In-Situ* Regression Algorithm

After AMSR is launched, purely statistical algorithms can be developed by collocating the AMSR T_B's with selected *in-situ* sites. A simple least-squares regression is then found that relates the *in situ* parameter to the T_B's. The mathematical form of this type of algorithm is identical to the linear regression algorithm given by (72). The difference is that the c_{ij} coefficients are not derived from radiative transfer theory, but rather from the regression to the *in situ* data. Examples of this type of algorithm are the *Goodberlet et al.* [1989] SSM/I wind algorithm and the *Alishouse et al.* [1990] SSM/I water vapor algorithm.

The strength of the purely statistical algorithm is that it does not require a radiative transfer model, and hence it is not affected by modeling errors. The weaknesses are:
1. The algorithm for AMSR cannot be developed until after launch.
2. Large *in situ* data sets covering the full range of global conditions must be assembled and collocated with the AMSR observations.

3. The purely statistical algorithm is keyed to specific sensor parameters such as frequency and incidence angle. For example, none of the algorithms developed for SSM/I can be applied to AMSR. In contrast, SSM/I algorithms based on radiative transfer theory can be interpolated to the new AMSR frequencies and incidence angle.

4. Cross-talk among the various geophysical parameters is a problem for the statistical algorithm. For example, consider sea-surface temperature T_S and water vapor V which are highly correlated on a global scale. A purely statistical algorithm will mimic this correlation and will generate a T_S product that is <u>always</u> highly correlated with V. In nature, when the true V changes and T_S remains constant (i.e., a weather system passing by), the statistical algorithm will erroneously report a change in T_S.

5. For the case of cloud water retrieval, for which there is no reliable *in situ* data, this type of algorithm cannot be used.

We think it is a mistake to ignore the physics when developing an algorithm. It may be the case that relatively simple regressions can be used to retrieve some of the parameters. However, it is important that these regressions be understood in the context of radiative transfer theory. Thus, after AMSR is launched and the collocated *in situ* data are available, we will calibrate the pre-launch algorithm by making small adjustments to the radiative transfer model rather than developing purely statistical algorithms. This calibration activity is discussed in the Section 5.

3.6. Incidence Angle Variations

The retrieval of sea-surface temperature and wind speed are sensitive to incidence angle variations. A 1° error in specifying θ_i produces a 6 C error in T_S and a 5 m/s error in W. Thus, it is crucial that the incidence angle be accurately known and that the retrieval algorithm accounts for incidence angle variations.

The pointing knowledge for the PM platform is specified to be 0.03°/axis. This figure is the 3-standard deviation error in the knowledge of the roll, pitch, and yaw. Yaw variations do not affect the incidence angle, but roll and pitch do. The corresponding 3-standard deviation error in incidence angle is approximately 0.05°. The retrieval accuracy for the geophysical parameters are in terms of a 1-standard deviation error, so we convert the incidence angle error to a 1-standard deviation error of 0.016°, and this results in a 0.1 C error in the T_S retrieval and a 0.1 m/s error in the W retrieval. The specification of pointing knowledge for the PM platform is, therefore, sufficient. However, the pointing knowledge of the AMSR instrument is yet to be specified. We will be paying close attention to this instrument specification.

In the non-linear, iterative algorithm, incidence angle is an explicit parameter in the model function, and hence θ_i variations are easily handled by simply assigning a value to θ_i before doing the inversion process. There are two possible methods for handling incidence angle variation in the linear regression algorithm. First, include incidence angle as an additional term in the regression or second, normalize the T_B's to some constant incidence angle, say 55°, before applying the regression. This normalization is expressed by

$$T_B\left(55^{\circ}\right) = T_B\left(\theta_i\right) + \mu \cdot \theta_i - 55^{\circ} \tag{83}$$

where μ represents the derivative $\partial T_B/\partial \theta_i$, which depends on the T_S, W, V, and L. We find that μ can be accurately approximated by a T_B regression of the type given by (73). This method works well when the incidence angle variations are ± 1° or less, which should be the case for AMSR.

6. References

Alishouse, J.C., S. Synder, J. Vongsathorn, and R.R. Ferraro, Determination of oceanic total precipitable water from the SSM/I, *IEEE Trans. Geoscience and Remote Sensing, 28*, 811-816, 1990.

Archer, D.G., and P. Wang, The dielectric constant of water and debye-huckel limiting law slopes, *J. Phys. Chem. Ref. Data, 19*, 371, 1990.

Becker, G.E., and S.H. Autler, Water vapor absorption of electromagnetic radiation in the centimeter wave-length range, *Phys. Rev., 70*(5/6), 303-307, 1946.

Cole, K.S., and R.H. Cole, Dispersion and absorption in dielectrics, *J. Chemical Physics, 9,* 341-351, 1941.

Cox, C.S., Measurements of slopes of high-frequency wind waves, *J. Mar. Res., 16*, 199-225, 1958.

Cox, C.S., and W.H. Munk, Measurement of the roughness of the sea surface from photographs of the sun's glitter, *J. Opt. Soc. Am., 44*, 838-850, 1954.

Debye, R., *Polar Molecules*, Chemical Catalog, New York, 1929.

Goldstein, H., Attenuation by condensed water, *Propagation of Short Radio Waves, MIT Rad. Lab. Ser., 13,* McGraw-Hill, New York: 1951.

Goodberlet, M.A., C.T. Swift, and J.C. Wilkerson, Remote sensing of ocean surface winds with the SSM/I, *J. Geophys. Res., 94*, 14547-14555, 1989.

Grant, E., T. Buchanan, and H. Cook, Dielectric behavior of water at microwave frequencies, *J. Chem. Phys., 26*, 156-161, 1957.

Haggis, G.H., J.B. Hasted, T.J. Buchanan, The dielectric properties of water in solutions, *J. Chem. Phys., 20*, 1452-1465, 1952.

Hasted, J.B., and S. El Sabeh, The dielectric properties of water in solutions, *Trans. Faraday Soc., 49*, 1003-1011, 1953.

Hasted, J.B., and G. Roderick, Dielectric properties of aqueous and alcoholic electrolytic solutions, *J. Chem. Phys., 29*, 17-26, 1958.

Ho, W., and W. F. Hall, Measurements of the dielectric properties of sea water and NaCl solutions at 2.65 GHz, *J. Geophys. Res., 78*, 6301-6315, 1973.

Ho, W.W., A.W. Love, and M. J. Van Melle, Measurements of the dielectric properties of sea water at 1.43 GHz, *NASA Contractor Report CR-2458*, 1974.

Jones, W.L., P.G. Black, D.M. Boggs, E.M. Bracalente, R.A. Brown,, G. Dome, J.A. Ernst, I.M. Halberstam, J.E. Overland, S. Peteherych, W.J. Pierson, F.J. Wentz, P.M. Woiceshyn, and M.G. Wurtele, Seasat scatterometer: Results of the Gulf of Alaska workshop, *Science, 204*, 1413-1415, 1979.

Keller, W.C., and J.W. Wright, Microwave scattering and the straining of wind-generated waves, *Radio Sci., 10*, 139-147, 1975.

Klein, L.A., and C.T. Swift, An improved model for the dielectric constant of sea water at microwave frequencies, *IEEE J. Oceanic Eng., OE-2*, 104-111, 1977.

Lane, J.A., and J.A. Saxton, Dielectric dispersion in pure polar liquids at very high frequencies, III. The effect of electrolytes in solution, Proc. Roy. Soc., A213, 531-545, 1952.

Lide, D.R, *Handbook of Chemistry and Physics, 74th Edition*, CRC Press, Ann Arbor, p. 6-10, 1993.

Liebe, H.J., An updated model for millimeter wave propagation in moist air, *Radio Sci., 20*, 1069-1089, 1985.

Malmberg, C., and A. Maryott, Dielectric constant of water from $0°$ to $100°C$, *J. Res. Nat. Bureau of Standards, 56*, 1-8, 1956.

Marshall, T.S., and W.McK. Palmer, The distribution of raindrops with size, *J. Meteor., 5*, 165-166, 1948.

Mitsuyasu, H., and T. Honda, Wind-induced growth of water waves, *J. Fluid Mech., 123*, 425-442, 1982.

Monahan, E.C., and I. O'Muircheartaigh, Optimal power-law description of oceanic whitecap coverage dependence on wind speed, *J. Phys. Oceanogr., 10*, 2094-2099, 1980.

Peake, W.H., Interaction of electromagnetic waves with some natural surfaces, *IEEE Trans. Antennas Propagat., AP-7*, S324-S329, 1959.

Reif, F., *Fundamentals of Statistical and Thermal Physics*, McGraw-Hill, Inc., San Francisco, p. 381-388, 1965.

Rice, S.O., Reflection of electromagnetic waves from slightly rough surfaces, *Commun. Pure Appl. Math, 4*, 351-378, 1951.

Rosenkranz, P.W., Shape of the 5 mm oxygen band in the atmosphere, *IEEE Tran. Antennas Propag., AP-23*(4), 498-506, 1975.

Smith, P.M., The emissivity of sea foam at 19 and 37 GHz, *IEEE Trans. Geosci. Remote Sensing, GE-26*, 541-547, 1988.

Stogryn, A., The apparent temperature of the sea at microwave frequencies, *IEEE Trans. Antennas Propagat., AP-15*, 278-286, 1967.

Stogryn, A., Equations for calculating the dielectric constant of saline water, *IEEE Trans. Microwave Theory Tech., MTT-19*, 733-736, 1971.

Stogryn, A., The emissivity of sea foam at microwave frequencies, *J. Geophys. Res., 77*, 1650-1666, 1972.

Waters, J.R., Absorption and emission by atmospheric gases, *in Methods of Experimental Physics*, vol. 12B, edited by M.L. Meeks, chap. 2.3, Academic, Orlando, Fla., 1976.

Wentz, F.J., A two-scale scattering model for foam-free sea microwave brightness temperatures, *J. Geophys. Res., 80*, 3441-3446, 1975.

Wentz, F.J., A model function for ocean microwave brightness temperatures, *J. Geophys. Res., 88*, 1892-1908, 1983.

Wentz, F.J., Measurement of oceanic wind vector using satellite microwave radiometers, *IEEE Trans. Geosci. and Remote Sensing, 30*, 960-972, 1992.

Wentz, F.J., A well-calibrated ocean algorithm for SSM/I, *J. Geophys. Res.,102*, 8703-8718, 1997.

Wentz, F.J., and R.W. Spencer, SSM/I rain retrievals within an unified all-weather ocean algorithm, *J. Atmospheric Science, 55*, 1613-1627, 1998.

Weyl, P.K., On the change in electrical conductance of sea water with temperature, *Limnol. Oceanogr., 9*, 75-78, 1964.

Wilheit, T.T., and A.T.C. Chang, An algorithm for retrieval of ocean surface and atmospheric parameters from the observations of the Scanning Multichannel Microwave Radiometer (SMMR), *Radio Science, 15,* 525-544, 1980.

Wu, S.T., and A.K. Fung, A non-coherent model for microwave emission and backscattering from the sea surface, *J. Geophys. Res., 77,* 5917-5929, 1972.

Yueh, S.H., W.J. Wilson, K. Li and and S.J. Dinardo, Polarimetric microwave brightness signatures of ocean wind directions, *IEEE Trans. Geosci. and Remote Sensing, 37,* 949-959, 1999.